Regulating Infrared Photoresponses in Reduced Graphene Oxide Phototransistors by Defect and Atomic Structure Control

Haixin Chang,[†,*] Zhenhua Sun,[‡] Mitsuhiro Saito,[†] Qinghong Yuan,[§] Han Zhang,[§] Jinhua Li,[‡] Zhongchang Wang,[†] Takeshi Fujita,[†] Feng Ding,[§] Zijian Zheng,[§] Feng Yan,[‡,*] Hongkai Wu,[†,⊥,*] Mingwei Chen,[†] and Yuichi Ikuhara[†,∥]

[†]WPI-Advanced Institute for Materials Research, Tohoku University, Sendai 980-8578, Japan, [‡]Department of Applied Physics, The Hong Kong Polytechnic University, Hong Kong, China, [§]Nanotechnology Centre, Institute of Textiles and Clothing, The Hong Kong Polytechnic University, Hong Kong, China, [⊥]Department of Chemistry, The Hong Kong University of Science and Technology, Hong Kong, China, and [∥]Institute of Engineering Innovation, The University of Tokyo, 2-11-16 Yayoi, Bunkyo-ku, Tokyo 113-8656, Japan. H.X.C., F.Y., and H.K.W. conceived and designed the experiments. H.X.C. prepared graphene and the devices. Z.H.S. and J.H.L. conducted the device measurements. Y.I., M.W.C., M.S., Z.C.W., and T.F. performed the TEM characterizations. Z.J.Z. helped with AFM measurements and initial studies. F.D., Q.H.Y., and H.Z. calculated the theoretical models. H.X.C., F.Y., and H.K.W. wrote the manuscript. All the authors commented on the manuscript.

ABSTRACT Defects play significant roles in properties of graphene and related device performances. Most studies of defects in graphene focus on their influences on electronic or luminescent optical properties, while controlling infrared optoelectronic performance of graphene by defect engineering remains a challenge. In the meantime, pristine graphene has very low infrared photoresponses of ~0.01 A/W due to fast photocarrier dynamics. Here we report regulating infrared photoresponses in reduced graphene oxide phototransistors by defect and atomic structure control for the first time. The infrared optoelectronic transport and photocurrent generation are significantly influenced and well controlled by oxygenous defects and structures in reduced graphene oxide. Moreover, remarkable infrared photoresponses are observed in photoconductor devices based on reduced graphene oxide with an external responsivity of ~0.7 A/W, at least over one order of magnitude higher than that from pristine graphene. External quantum efficiencies of infrared devices reach ultrahigh values of ~97%, which to our knowledge is one of the best efficiencies for infrared photoresponses from nonhybrid, pure graphene or graphene-based derivatives. The flexible infrared photoconductor devices demonstrate no photoresponse degradation even after 1000 bending tests. The results open up new routes to control optoelectronic behaviors of graphene for high-performance devices.

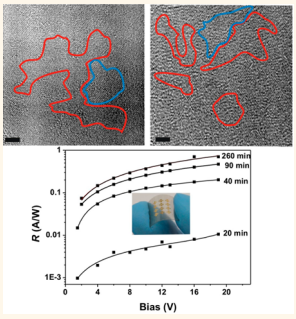

KEYWORDS: reduced graphene oxide · defect · infrared · photoresponse · phototransistor

Defects play significant roles in the properties of graphene and related device performance.[1−3] Most studies on the defects in graphene-based materials focus on their influence on the electronic aspects.[4−15] Besides electronic properties, graphene also has unique optical properties enabling many fundamental and practical optical and optoelectronic applications.[16−41] Graphene absorbs ~2.3% in the very broad wavelength for a single-layer sheet.[16] The peculiar combinations of extraordinary photonic and electronic properties of graphene (*e.g.*, linear energy dispersion crossing at the Dirac point and ultrahigh carrier mobility) have inspired novel photonic and optoelectronic devices, which are limited in conventional material systems.[1,3] Very recently, infrared graphene photodetectors with optical modulation up to 40 GHz have been demonstrated based on pristine graphene but with a very low responsivity of 6.1 mA/W due to fast photocarrier dynamics.[21,22] Graphene also shows gate-tunable optical absorption,[17] ballistic photocurrent generation,[33] broadband polarization,[31] giant Faraday rotation,[34] hot carrier effects,[30,35,41] and photothermoelectric effects.[40] However, although some work emphasized the influence of defects on some optical properties, mostly luminescence,[42,43] the influences of defects on optoelectronic behaviors in

* Address correspondence to hxchang@wpi-aimr.tohoku.ac.jp; apafyan@polyu.edu.hk; chhkwu@ust.hk.

Received for review May 10, 2013 and accepted June 19, 2013.

Published online June 19, 2013
10.1021/nn4023679

graphene-based materials are rarely investigated, especially for infrared photoresponses, which have great importance in modern optoelectronics.[21,22,35] Because of the complexity of defects, controlling the infrared optoelectronic performance of graphene devices by defect engineering remains a challenge.

To address the challenge, here we report regulating infrared photoresponses in reduced graphene oxide phototransistors by defect and atomic structure control for the first time. The infrared optoelectronic transport behaviors and photocurrent generation in solution-processable, few-layer reduced graphene oxide (FRGO) semiconductors were significantly influenced and thus well controlled by oxygenous defects and structure in reduced graphene oxide. Moreover, FRGO with controlled defects was readily applied as infrared optoelectronic elements such as photoconductor devices with a remarkable infrared photoresponse (at 895 nm) of ~0.7 A/W, at least over one order of magnitude higher than that from pristine graphene. External quantum efficiencies (EQE) of infrared devices reached an ultrahigh value of ~97%, which to our knowledge is one of the best efficiencies for infrared photoresponses from nonhybrid, pure graphene or graphene derivatives. Patterned FRGO photoconductor devices also demonstrated ultrahigh flexible performance with no photoresponse degradation even after 1000 bending tests. The results hereby open up new routes to control infrared optoelectronic behaviors of graphene for high-performance devices.

RESULTS AND DISCUSSION

Reduced graphene oxide was obtained by thermal reduction of exfoliated graphene oxide (more details in the Methods and Supporting Information). The morphology, microstructure, and chemical functional groups in graphene oxide and reduced graphene oxide were characterized and monitored by atomic force microscopy (AFM, Figure 1), transmission electron microscopy (TEM, Figure 1), and X-ray photoelectron spectra (XPS, Figure 1 and Figure 2). Single-layer graphene oxide was ~1.2 nm thick (Figure 1a), which is typical for single-layer one,[14,24] and was further confirmed by TEM electronic diffraction (supplementary

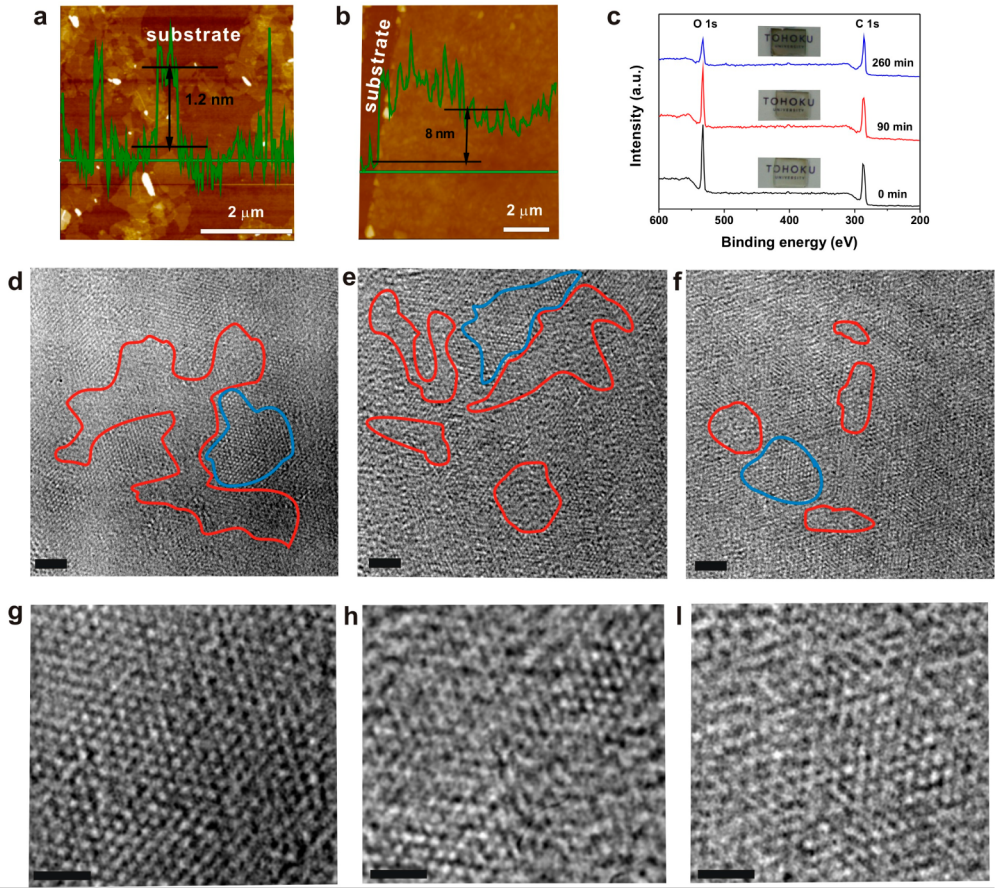

Figure 1. Characterizations of graphene oxide and reduced graphene oxide. AFM images and height profiles for single-layer graphene oxide (a) and few-layer graphene oxide film (b) on SiO_2/Si substrate. (c) XPS spectra of few-layer graphene oxide films after thermal reduction times of 0, 90, and 260 min. Inset: The resulting films on glass substrates (~1 cm^2). TEM images showing structural evolution of graphene oxide (d) and 90 min (e) and 260 min (f) thermally reduced graphene oxide. Red line defines an area of highly disordered structure. Blue line defines an area of relatively ordered structure. The images in d–f were low-pass filtered to remove noise. Scale bars in d, e, and f are 2 nm. (g–i) Enlarged view of blue line defined areas in d, e, and f, respectively. Scale bars in g, h, and i are 1 nm.

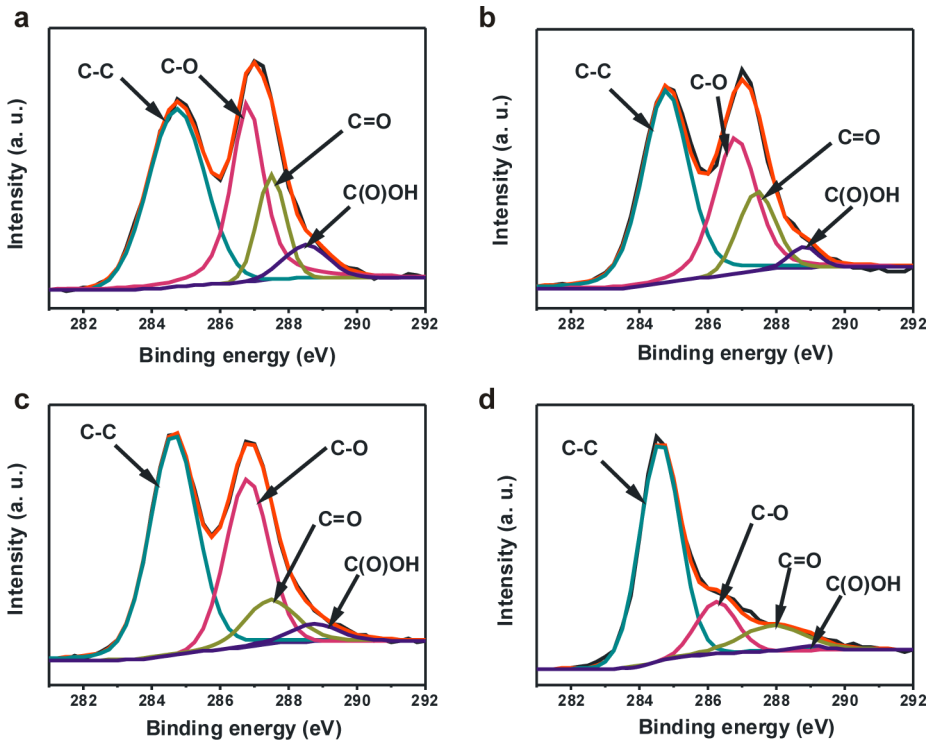

Figure 2. C 1s XPS spectra for graphene oxide and 20, 90, and 260 min reduced graphene oxide. (a) Graphene oxide, (b) 20 min reduced graphene oxide, (c) 90 min reduced graphene oxide, (d) 260 min reduced graphene oxide.

Figure S1). The large area, few-layer graphene oxide film was then fabricated from single-layer graphene oxide. The obtained continuous few-layer graphene oxide (FGO) film was ~8 nm thick on average, which is less than eight layers considering the thickness of 1.2 nm for single-layer graphene oxide (Figure 1b). The film was then thermally reduced at a very low temperature of 150 °C for different periods up to 260 min. The Raman mapping of the G peak (~1600 cm^{-1}) shows the continuity of FRGO in a large area (supplementary Figure S2). The G peak in FRGO had no shift in peak center position compared with FGO, but had narrower full widths at half-maximum (fwhm) after thermal treatments for 90 min (73 cm^{-1}) and 260 min (76 cm^{-1}) than that in FGO (84 cm^{-1}). More importantly, the oxygenous defects, *i.e.*, the oxygenous functional groups, in FRGO can be tuned with good control by the low-temperature thermal reductions, as demonstrated by X-ray photoelectron spectra (XPS) (Figure 1c and Figure 2). For example, the amounts of oxygenous defects in FRGO decrease over 50% within a 260 min reduction, resulting in the reduction of transmittance (inset in Figure 1c). The O/C atomic ratio decreased from ~0.5 in graphene oxide to ~0.46 in 20 min reduced graphene oxide, ~0.4 in 90 min reduced FRGO, and ~0.25 in 260 min reduced FRGO. More changes of oxygenous defects can be obtained by multipeak fitting of C 1s spectra (Figure 2). The C−C bond (~284.5 eV) still largely exists in all the samples. The C−O bond (~286.5 eV) is the main oxygenous species in graphene oxide with fewer C═O (~287.5 eV) and C(O)OH (~289 eV), consistent with previous studies.[44−46] In addition, the C−O bond decreased significantly during the reduction process.[44−46] The fraction of sp^2 carbon, roughly estimated from the C−C bond, was ~46% in graphene oxide and ~49%, 52%, and 69% in 20, 90, and 260 min reduced graphene oxide, respectively, when considering them as sp^2/sp^3 complex systems.[44] The reduction of graphene oxide at low temperature is due to the thermal dissociation of oxygenous groups at over 100 °C by forming H_2O, CO, or CO_2.[45,47] Moreover, the band gap of reduced graphene oxide can be tuned in a wide range by controlling the oxygenous content.[15,24,42,48] For instance, reduced graphene oxides obtained by 20, 90, and 260 min thermal reduction have optical band gaps of ~1.5, 1, and 0.5 eV, respectively, while the band gap for graphene oxide is ~2.2 eV, which are roughly determined from optical absorption methods.[24,49] These kinds of FRGO semiconductors may be infrared responsive due to their relatively low oxygenous content.

The atomic structure evolution of graphene oxide under low-temperature thermal reduction was further investigated. It has been a big challenge to control the atomic structure in reduced graphene oxide. Oxygenous defects destroy the ordered hexagonal lattice of graphene in the chemical oxidization process and form disordered structures even after reduction.[46−48] In general, the structure of graphene oxide is believed to be transformed to more ordered structures due to restoration of conjugation after reduction. However, importantly, the evolution of atomic structures in

graphene oxide was more complicated than expected when thermally reduced. The atomic structure changes were bidirectional evolution, where both highly ordered and highly disordered areas in graphene oxide changed (Figure 1d–i and supplementary Figures S3 and S4). Original graphene oxide had both a large amount of continuous, highly disordered areas with many oxygenous defects (*e.g.*, red line defined areas, Figure 1d) and a large amount of highly ordered areas with few oxygenous defects (*e.g.*, blue line defined area in Figure 1d and enlarged view in Figure 1g). The continuous, highly disordered areas in graphene oxide shrank to smaller highly disordered areas after 90 min of thermal reduction (Figure 1e) and to much smaller, fully separate, highly disordered areas after 260 min of thermal reduction (Figure 1f). The changes, on one hand, made reduced graphene oxide much less disordered than graphene oxide in general. On the other hand, no large amount of highly ordered areas, like that in graphene oxide (Figure 1g), was observed in 90 and 260 min reduced graphene oxide. Instead, relatively ordered structures with strong distortion were found (blue line defined area in Figure 1e,f and enlarged view in Figure 1h,i). This unique structural evolution resulted in unprecedented heterogeneous structures in reduced graphene oxide with very different quantities of oxygenous defects from area to area (Figure 1e,f). The structural evolution was further confirmed by selected-area electron diffractions (supplementary Figure S4). The diffraction spots in graphene oxide showed very clear hexagonal symmetry. However, the diffraction spots in reduced graphene oxide (both 90 and 260 min reduction) tended to be lengthened and formed an amorphous-like ring. The observed structural changes are also consistent with the changes in local chemical bonding states, as shown in C 1s XPS spectra (Figure 2). For example, the decrease of oxygenous functional groups was observed with the increase of the reduction time, which resulted in a gradual increase of C–C bonding fractions (Figure 2).[44–46] In particular, C–O bonds decreased obviously (over 50%) in the 260 min reduction, while C=O and C(O)OH undergo only a slight change (Figure 2d). When considering graphene oxide and reduced graphene oxide as a complex of sp^2/sp^3 system,[44] the fractions of sp^3 carbon (induced mainly by bonded oxygenous functional groups) decreased from ~54% for graphene oxide to ~48% and 31% for 90 and 260 min reduced graphene oxide, respectively. The reason for this structural change is that the oxygenous functional groups are removed and the conjugations between carbon atoms recover gradually during the reduction.[44–46] The impact of this structure evolution on infrared optoelectronic transport properties in reduced graphene oxide was investigated by field effect phototransistor measurements.

The standard back-gated field effect devices were then fabricated based on FRGO semiconductors

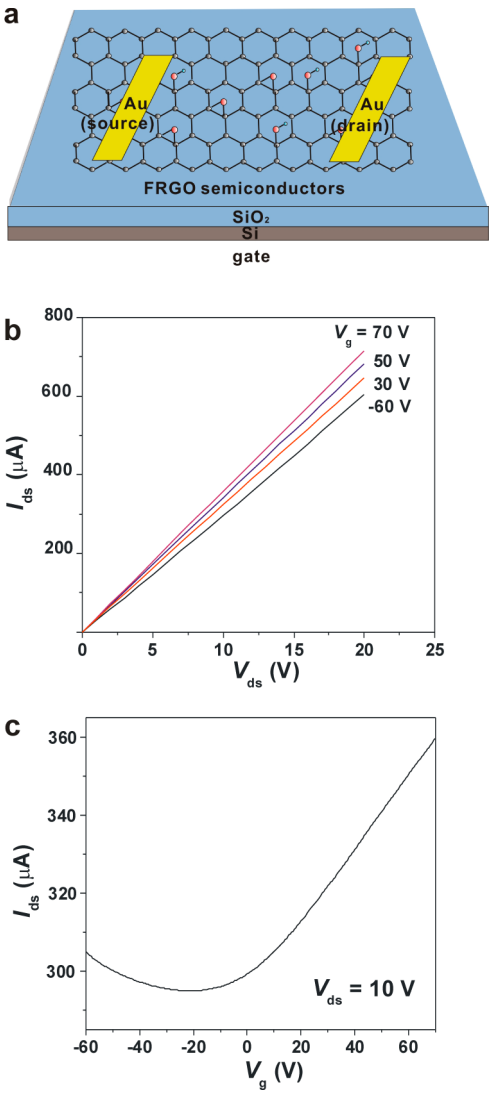

Figure 3. Electronic transport properties of FRGO-based FETs. (a) Scheme for a FRGO FET. (b) I_{ds}–V_{ds} curves with V_g of 70, 50, 30, and −60 V. (c) I_{ds}–V_g curve of FRGO FETs with V_{ds} of 10 V. Reduction time for FRGO is 90 min.

(Figure 3a). Due to solution-processable capability, large-scale thin-film transistor fabrication can be easily achieved with high throughput (supplementary Figure S5). Electronic transport characteristics of FRGO FETs were then investigated (Figure 3b,c). Obvious dependence of source–drain current (I_{ds}) on the gate voltages was observed (Figure 3b,c). The transport measurements demonstrated bipolar characteristics, with the minimum conductance achieved at a gate voltage of ~−20 V (Figure 3c), typical for mono- and few-layer graphene-based materials. Note that a field effect was found only in 90 and 260 min FRGO semiconductors. No obvious field effect (supplementary Figure S6a) was observed in FGO and FRGO with short reduction time (*e.g.*, 20 and 40 min) because of the large quantity of oxygenous defects (Figure 1c,d and Figure 2).

To investigate the influences of oxygenous defects and structures on infrared optoelectronic transport

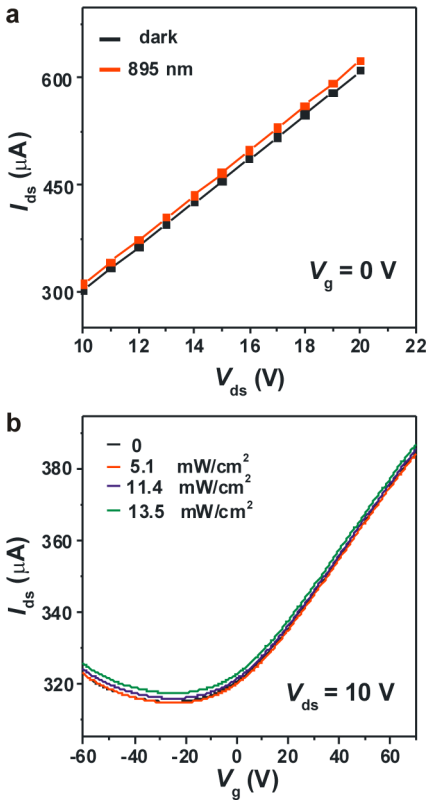

Figure 4. Infrared photoresponses of 90 min FRGO FETs. (a) I_{ds}−V_{ds} curves of FRGO under dark and incident radiation power of 13.5 mW/cm^2 without gate voltage. (b) I_{ds}−V_g curves of FRGO FETs under different incident powers with V_{ds} = 10 V.

properties of photocarriers in FRGO, we studied the infrared photoresponses of FETs based on FGO and two kinds of FRGO. No obvious photocurrent generation and decay were observed in FGO (supplementary Figure S6b−d). For 90 min FRGO, a clear photocurrent generation was observed after infrared radiation (895 nm, Figure 4a). Gate voltage-dependent measurements of infrared photoresponses revealed more details. The hole current under a negative gate voltage of −60 V increased monotonically with the incident radiation intensities, while the electron current under a positive gate voltage of 70 V decreased at low light intensity (*e.g.*, 5.1 and 9.4 mW/cm^2) and increased in higher light intensities (over 11.4 mW/cm^2) (Figure 4b, Figure 5a−d). Note that no obvious changes in gate voltage at minimum conductance (supplementary Figure S7a) and mobility of charge carriers (Figure 4b, Figure 5a,b) were observed in 90 min FRGO under infrared radiation.

A different infrared response was found in 260 min FRGO FETs. Although clear infrared photocurrent generations were also observed similar to 90 min FRGO (Figure 6a), gate voltage-dependent measurements of the photoresponses showed a different characteristic from 90 min FRGO. Both the hole current under a negative gate voltage of −60 V and electron current under a positive gate voltage of 70 V increased monotonically with the incident light intensities (Figure 6b, Figure 7a−d). No obvious changes in gate voltage at minimum conductance (supplementary Figure S7b) and mobility of charge carriers (Figure 6b, Figure 7a,b) were observed in 260 min FRGO under infrared radiation, similar to that in 90 min FRGO.

We further plotted the source−drain current *versus* incident light intensities under a gate voltage of −60 and 70 V, respectively, for 90 and 260 min FRGO. For 90 min FRGO, the fitted curve of photocurrent under 70 V gate voltage can be described as $I_{ds} = 384.95 + 0.7w - 9.0(1 - \exp(-0.13w))$ (Figure 5d), where I_{ds} has a unit of μA and w is the infrared light intensities with a unit of mW/cm^2; 384.95 is the output current of the device in the dark. The linear term, $0.7w$, is the photogenerated electron current under infrared radiation. The nonlinear term $-9.0(1 - \exp(-0.13w))$ can be explained with electron trapping induced by oxygenous defects in FRGO, which will be discussed in more detail together with the first-principles calculations later (supplementary Figure S8). As for the photogenerated hole current under a gate voltage of −60 V in 90 min FRGO, the slope in the linear range is ~0.61 (Figure 5c), which is close to the fitted coefficient of 0.7 in the linear term, $0.7w$, for photogenerated electron current (Figure 5d). It is consistent with the fact that the photogeneration efficiencies for the holes and electrons under radiation should be the same for a sample. As for 260 min FRGO, the slope for the photocurrent generation in the linear range is ~1.12 and 1.05 for hole current and electron current (Figure 7c,d), respectively. The photocurrent generation capability (photocurrent per unit radiation power and source−drain bias) calculated from the slopes in the photogenerated hole currents, like that in Figures 5c and 7c, is ~49.3 mA/W V for 260 min FRGO, which is ~2.3 times that for 90 min FRGO (Figure 7e).

First-principles calculations were performed to better understand the influence of oxygenous defects on the infrared photoresponses of FRGO. Graphene oxide will be transformed to reduced graphene of less oxygenous defects after reduction with most oxygeous defects as epoxy and hydroxyl defects.[44−46] First-principles models of reduced graphene oxide with different oxygenous contents, $C_{40}O_{12}H_6$ and $C_{40}O_8H_6$, were then built based on XPS measurements (Figure 2) and recent experimental and theoretical investigations (supplementary Figure S8; see more details about theoretical models in the Supporting Information).[44−48] The highest occupied molecular orbital (HOMO), lowest unoccupied molecular orbital (LUMO), and the first vertical excitation energy for reduced graphene oxide clusters with different oxygenous defects were calculated using methods based on density functional theory similar to previous studies.[50−52] The calculations indicate the strong relation of first vertical excitation energy with oxygenous defects and the possibility of excited

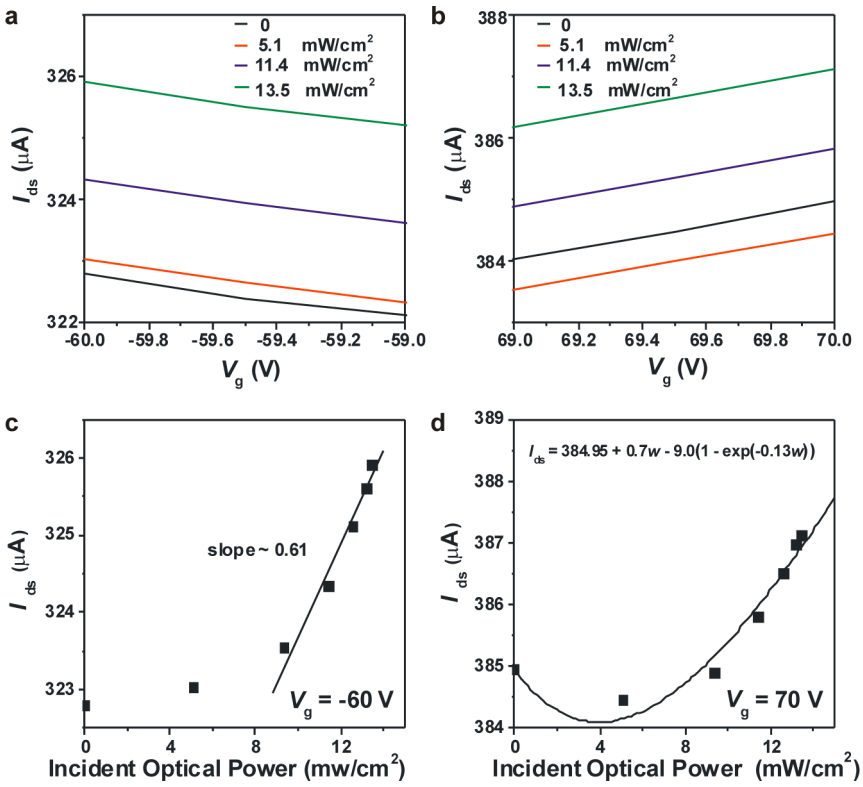

Figure 5. (a) Enlarged view of Figure 4b at a gate voltage from −60 to −59 V. (b) Enlarged view of Figure 4b at a gate voltage of 69−70 V. Plot and fitting of I_{ds} at $V_g = -60$ V (c) and $V_g = 70$ V (d) *versus* incident power. Inset in d: The fitted equation for I_{ds} (μA) *versus* incident power, where w is the incident power (mW/cm^2). Effective channel area for the device is ~0.2 mm^2.

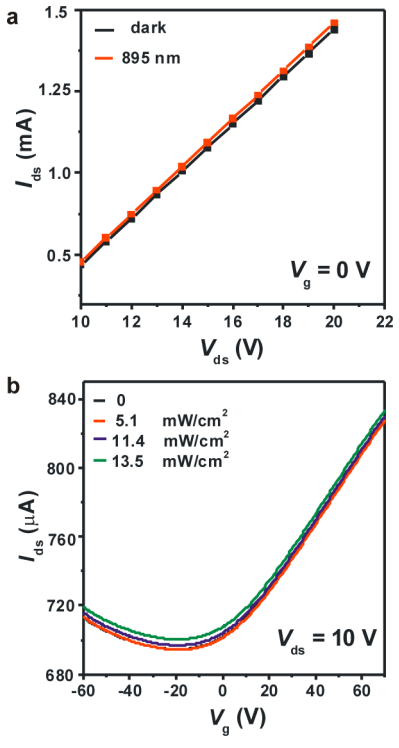

Figure 6. Infrared photoresponses of 260 min FRGO FETs. (a) $I_{ds}-V_{ds}$ curves of FRGO FETs under dark and incident radiation power of 13.5 mW/cm^2 without gate voltage. (b) $I_{ds}-V_g$ curves of FRGO FETs under different incident powers with $V_{ds} = 10$ V.

states induced by infrared radiations in reduced graphene oxide. Oxygenous defects in graphene are known electron trapping centers,[53] and the direct result of the above-mentioned excitations is that some electrons in reduced graphene oxide are trapped by the oxygenous defects. The trapping of electrons in excited states results in the reduction of electron carrier density at low radiation intensity. Such electron trapping will become saturated when all oxygenous defects are excited under high radiation intensity, followed by much stronger generation of photocarriers than that at low radiation intensity. Hence the linear increase of photocurrent *versus* radiation intensity recovers at higher radiation intensity. This is consistent with the observed photoresponses in 90 and 260 min FRGO. Such nonmonotonic optoelectronic behaviors disappeared when oxygenous defects decrease significantly with much weaker electron trapping, as evidenced in the 260 min FRGO. Note that there was no obvious decrease of hole current in both 90 and 260 min FRGO upon infrared excitation.

The oxygenous defects also affected the time-resolved photoresponses in 90 and 260 min FRGO. A quick photocurrent increase was followed by a slow increase under infrared radiations for both 90 min (supplementary Figure S9) and 260 min (supplementary Figure S10) FRGO. The photocurrent generation curves can be fitted by a two-stage exponential curve with the form $I(t) = I_0 + A_1 \exp(-(t - t_0)/t_1) + B_1$

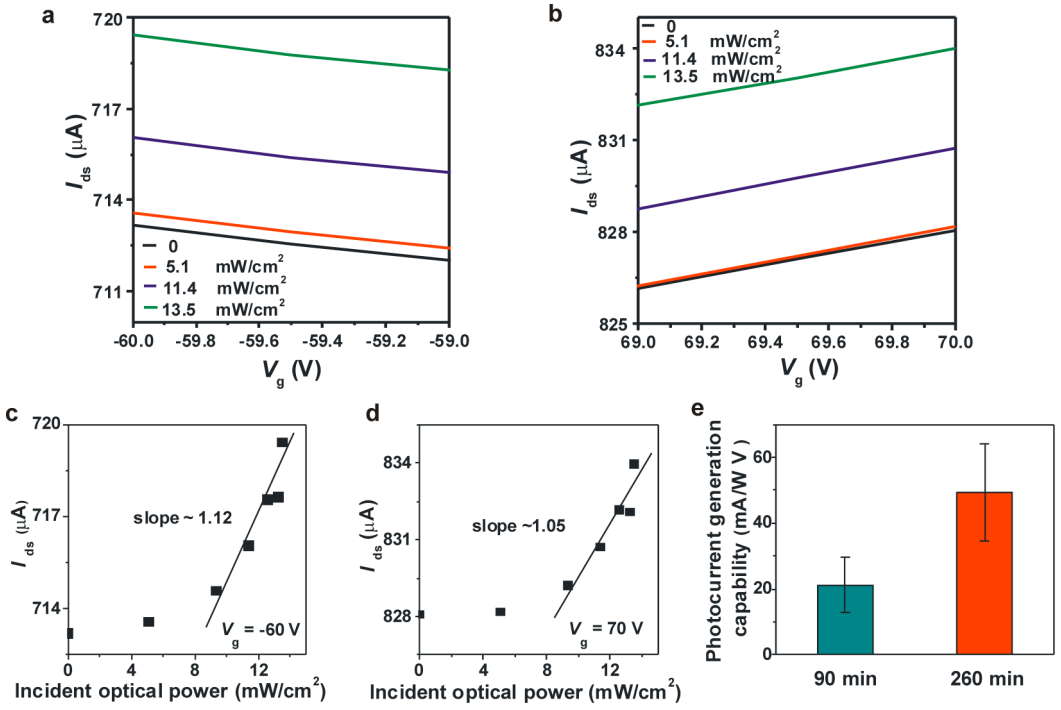

Figure 7. (a) Enlarged view od Figure 6b at a gate voltage from −60 to −59 V. (b) Enlarged view of Figure 6b at a gate voltages of 69−70 V. Plot and fitting of I_{ds} at V_g = −60 V (c) and V_g = 70 V (d) *versus* incident power. (e) Photocurrent generation capability (photocurrent per unit radiation power and source−drain bias) for 90 and 260 min FRGO calculated from slopes for photogenerated hole currents like that in Figure 5c and panel c. Effective channel area for a device is ~0.2 mm^2.

exp(−(*t* − t_0)/t_2), where I_0 and t_0 are constants and t_1 and t_2 are time parameters for photocurrent generation. The t_1 for both 90 and 260 min were 2 s. The t_2 for 90 and 260 min FRGO were 52 and 20 s, respectively. For the photocurrent decay curves, a quick decay was followed by a slow decay for 90 and 260 min FRGO. Similarly, the decay curves can also be fitted by a two-stage exponential curve: $I(t) = I_0' + A_2 \exp(-(t - t_0')/t_3) + B_2 \exp(-(t - t_0')/t_4)$, where I_0' and t_0' are constants, t_3 and t_4 are time parameters for photocurrent decay, t_3 for both 90 and 260 min FRGO were 6 s, and t_4 for 90 and 260 min FRGO were 242 and 90 s, respectively. Both photocurrent-generation saturation time t_2 and photocurrent decay time t_4 in 90 min FRGO were ~2.6 times that in 260 min FRGO, indicating the strong influence of oxygenous defects on the dynamics of photocarriers. The longer response time in 90 min FRGO than that in 260 min FRGO is induced by a larger amount of oxygenous defects and deep trap states that influence both photocarrier transport and recombination since oxygenous defects are known electron trapping centers.[53] We note that no obvious photocurrent generation or decay was observed in the time-resolved photoresponses of FGO (supplementary Figure S6c,d). The response rate for both kinds of FRGO was slower than for pure graphene (tens of picoseconds)[21,22] and makes FRGO unsuitable for ultrafast applications. The slow response in FRGO compared with graphene is the effect of residual oxygenous defects and resulting consequences on photocarrier transport and recombination. But FRGO has the advantage of high photoresponses and can be applied where ultrafast responses are not required. For example, one of the potential applications is gas sensors based on detecting the changes of infrared radiation after gas infrared absorption. Highly sensitive infrared photodetectors can also be used in some scientific applications, such as the observation of the universe structure through special telescopes. The response time is not the essential parameter for these applications, where slow responses are acceptable and the responsivity of photodetectors will be of most concern.

FRGO with controlled defects can be readily applied as optoelectronic elements such as photoconductor devices (Figure 8). For example, FRGO on SiO_2/Si was patterned by separated gold electrodes for conventional rigid photoconductor devices (inset in Figure 8b). The results indicated that the infrared photoresponses of FRGO photoconductor devices were strongly influenced by oxygenous defects (Figure 8a). Considering the geometry of the devices, the external infrared responsivity (*R*, A/W) can be described by the photocurrent generation per unit power of light and is given by

$$R = I_{ph}/(wS) \quad (1)$$

where I_{ph} is the photocurrent (the difference of source−drain currents under radiation and in the dark in I_{ds}−V_{ds} measurements such as Figure 4a and Figure 6a), *w* is the incident light intensity, and *S* is the effective area of the devices (0.2 mm^2).[21,22] The external quantum efficiency,

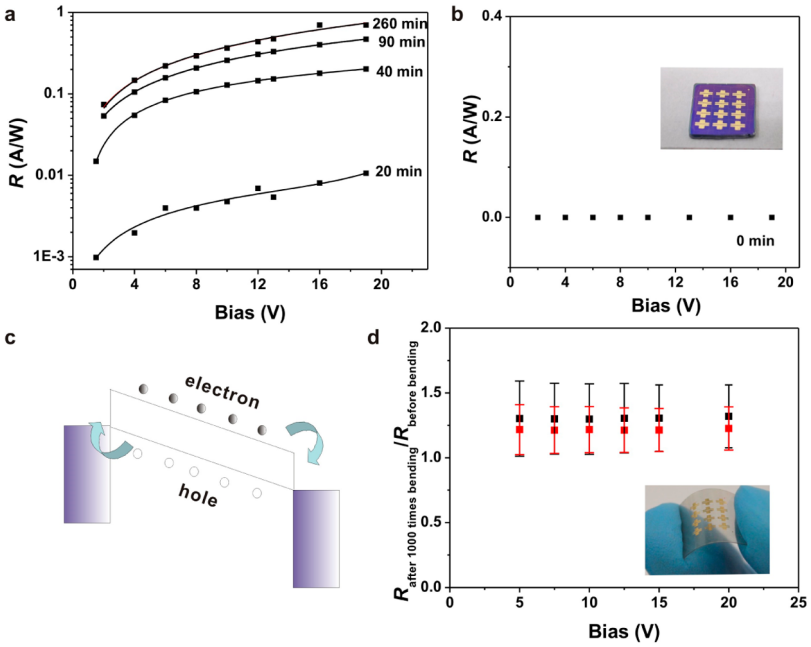

Figure 8. FRGO for rigid and flexible infrared photoconductor devices. (a, b) Responsivity *versus* bias for FRGO/SiO_2/Si-based rigid infrared photoconductor devices based on FRGO with different reduction times (0, 20, 40, 90, 260 min). Incident radiation power is ~14 mW/cm^2. Black lines in a are fitted curves. Inset in b: Digital image of rigid FRGO infrared photoconductor. (c) Schematic demonstration of photocarrier transport in FRGO under bias. (d) Ratio of responsivity for 260 min FRGO/PET flexible photoconductor devices after 1000 bending events to that before bending at different bias and radiation power. Black square is ~14 mW/cm^2; red square is ~21 mW/cm^2. Inset in d: Digital image of flexible FRGO infrared photoconductor.

i.e., external gain, can be calculated from

$$\mathrm{EQE} = hcR/(e\lambda) \qquad (2)$$

where h is Planck's constant, c the velocity of light, e the charge of an electron, and λ the wavelength of incident infrared radiation (895 nm in this work).[54,55] The gain of photoconductor devices is related to the photogenerated electron−hole pairs and the following photocarrier separation and transport under a certain bias (Figure 8c). A photoconductor can have a high gain if carriers can circulate in the conductor between two electrodes many times before they recombine with opposite charges. The photocurrent decay times (t_3, t_4) that represent the recombination rate of photocarriers in our FRGO phototransistors are much longer than those (tens of picoseconds) observed in pristine graphene phototransistors.[21,22] So a much higher gain in our FRGO phototransistor is expected.

The infrared photoresponse of FRGO photoconductor devices can be well modulated by reduction time (Figure 8). No obvious infrared responsivity was observed in FGO photoconductor devices (Figure 8b). Relatively small infrared photoresponse is observed in 20 and 40 min FRGO, moderate response in 90 min FRGO, and high response in 260 min FRGO. For example, the responsivity is ~0.01 A/W for 20 min FRGO and ~0.7 A/W for 260 min reduced FRGO at 19 V (Figure 8a). The small photocurrents in FGO and 20 and 40 min FRGO are consistent with field effect measurements where no obvious field effects were usually found due to very strong influences of oxygenous defects on the transport of charge carriers. The photoresponse trend in responsivity of the photoconductor devices is also consistent with the defect and atomic structures observed (Figure 1d−i): no responsivity in graphene oxide with large-scale, continuous highly disordered areas (Figure 1d), moderate responsivity in 90 min reduced graphene oxide with shrunken, smaller highly disordered areas (Figure 1e), and highest responsivity in 260 min reduced graphene oxide with fully separated, very small highly disordered areas (Figure 1f). However, this does not mean fewer defects are always better for infrared photoresponses. There were only very tiny, at least several tens-fold lower infrared responses observed in the high-quality chemical vapor deposition (CVD) graphene than that in FRGO under the same device configuration, bias, and radiation power as shown in supplementary Figure S11, consistent with previous studies.[56] The highest EQE of the FRGO infrared devices reached an ultrahigh ~97% in 260 min FRGO, which is one of the best efficiencies for infrared photoresponses from nonhybrid, pure graphene or graphene derivatives. The FRGO infrared devices have over 1 order of magnitude higher responsivity and EQE than infrared devices based on chemically, highly reduced graphene oxide[54] and have comparable performance with infrared devices based on graphene nanoribbons.[54] The ultrahigh EQE in 260 min FRGO was also partly attributed to optimized, moderate oxygenous defects and well-controlled

structures achieved by low-temperature reduction, which resulted in slow photocarrier recombination and acceptable photocarrier transport.[53]

Another intriguing property of FRGO-based photoconductor devices is its ultrahigh flexible performance. As a demonstration, flexible FRGO was fabricated on polyethylene terephthalate (PET) with a size at least as large as 13 cm diagonally (supplementary Figure S12a–c). FRGO was so flexible that it was folded even multiple times around one pen (Figure S12c). Moreover, patterned FRGO-based flexible infrared photoconductor devices (inset in Figure 8d) showed no obvious degradation of responsivity in different bias and both ~14 and ~21 mW/cm^2 infrared radiations even after 1000 bending tests (Figure 8d). This indicated great potential of FRGO in next-generation flexible optoelectronic elements. We note that FRGO is transparent (supplementary Figure S12a,b). The whole FRGO photoconductor device can be transparent when using transparent electrodes instead of gold, implying the applications in fully transparent and flexible devices.

CONCLUSION

We have reported regulating infrared photoresponses in reduced graphene oxide phototransistors by defect and atomic structure control. The oxygenous defects had a profound influence on the infrared photoresponses of FRGO and related infrared optoelectronic devices. The studies indicate that defects may play a significant role in the infrared optoelectronic behaviors of other graphene-based materials and devices, which could be well controlled by defect engineering. The remarkable infrared photoresponses of FRGO open up new possibilities to design efficient infrared optoelectronic devices for various applications considering that such chemically derived graphene is available by the ton.[57] The solution-processable, high-throughput, on-chip integration of nanometer-thick FRGO is compatible with current mature silicon semiconductor processing technology. Moreover, FRGO provides a general platform for large-scale, transparent, and flexible infrared optoelectronics and photonics where conventional rigid devices cannot work.

METHODS

Synthesis of Single-Layer Graphene Oxide and FRGO Films. Single-layer graphene oxide was prepared as reported elsewhere (see more details in Materials and Methods in the Supporting Information).[24,25,27,45] Typically, single-layer graphene oxide aqueous solutions (40 μL for a ~1 cm^2 substrate, ~0.3 mg/mL) were used to coat SiO_2/Si substrates by drop-casting. The substrates were cleaned for 30 s using oxygen plasma with 10 W power before the solution coating. The obtained few-layer graphene oxide films were annealed at 150 °C for different periods of time up to 260 min to control the content of oxygenous defects.

Characterizations. All the TEM imaging was conducted with TITAN 80-300 (FEI Company, The Netherlands) including a CEOS spherical aberration corrector and a Gatan Tridiem imaging filter at 80 kV accelerated voltage unless noted otherwise. XPS spectra were collected by a PHI Quantum 2000 X-ray photoelectron spectrometer. Large-scale Raman mapping was done with a Raman-11 laser Raman microscope (Nanophoton Co., Japan) under 540 nm excitation.

Fabrication and Photoresponse Measurement for Field Effect and Photoconductor Devices. The FRGO films on p-type highly doped silicon substrates with ~300 nm SiO_2 or on PET were patterned by gold electrodes with a channel length of 100 μm and width of 2 mm. The FETs were measured with an Agilent 4156C Precision semiconductor parameter analyzer (Agilent, USA) in a glovebox saturated with a nitrogen atmosphere at room temperature. The devices were stabilized overnight in the glovebox under dark in a nitrogen atmosphere. The device measuring system was kept in a sheltered dark environment to exclude interference from other light during the whole measurement. The infrared light was provided by an infrared light-emitting diode (LED) with an emission centered at ~895 nm. The FRGO FETs were radiated with infrared light of different incident intensities for 2 min to saturate the photoexcitation before taking the measurements. The incident light intensity was calculated and corrected by a Newport 2936-C dual-channel high-performance optical power and energy meter (Newport, USA). In the flexible device performance test, the patterned FRGO/PET photoconductor device (1 cm by 1 cm, PET thickness ~150 μm) was pressed to a radius of 7 mm followed by release. The bending was repeated up to 1000 times.[58]

First-Principles Theoretical Calculations. First-principles theoretical calculations were performed using density functional theory (DFT)-based methods similar to previous studies (more details in the Supporting Information).[50–52]

Conflict of Interest: The authors declare no competing financial interest.

Supporting Information Available: Materials and methods, first-principles calculations, supplementary Figure S1–S12, and supplementary references. This material is available free of charge *via* the Internet at http://pubs.acs.org.

Acknowledgment. This work was supported by World Premier International Research Center Initiative (WPI), MEXT, Japan. H.X.C. acknowledges the WPI-AIMR fusion research funding from MEXT and a Grant-in-Aid for Young Scientists B from JSPS (No. 25870057), Japan. F.Y. and Z.H.S. acknowledge the Research Grants Council (RGC) of Hong Kong, China (project: PolyU5322/10E), for financial support.

REFERENCES AND NOTES

1. Geim, A. K.; Novoselov, K. S. The Rise of Graphene. *Nat. Mater.* **2007**, *6*, 183–191.
2. Geim, A. K. Graphene: Status and Prospects. *Science* **2009**, *324*, 1530–1534.
3. Du, X.; Skachko, I.; Barker, A.; Andrei, E. Y. Approaching Ballistic Transport in Suspended Graphene. *Nat. Nanotechnol.* **2008**, *3*, 491–495.
4. Li, X. L.; Wang, X. R.; Zhang, L.; Lee, S. W.; Dai, H. J. Chemically Derived, Ultrasmooth Graphene Nanoribbon Semiconductors. *Science* **2008**, *319*, 1229–1232.
5. Kosynkin, D. V.; Higginbotham, A. L.; Sinitskii, A.; Lomeda, J. R.; Dimiev, A.; Price, B. K.; Tour, J. M. Longitudinal Unzipping of Carbon Nanotubes to Form Graphene Nanoribbons. *Nature* **2009**, *458*, 872–876.
6. Jia, X. T.; Hofmann, M.; Meunier, V.; Sumpter, B. G.; Campos-Delgado, J.; Romo-Herrera, J. M.; Son, H. B.; Hsieh, Y. P.; Reina, A.; Kong, J.; *et al.* Controlled Formation of Sharp Zigzag and Armchair Edges in Graphitic Nanoribbons. *Science* **2009**, *323*, 1701–1705.

7. Bai, J. W.; Zhong, X.; Jiang, S.; Huang, Y.; Duan, X. F. Graphene Nanomesh. *Nat. Nanotechnol.* **2010**, *5*, 190–194.
8. Ritter, K. A.; Lyding, J. W. The Influence of Edge Structure on the Electronic Properties of Graphene Quantum Dots and Nanoribbons. *Nat. Mater.* **2009**, *8*, 235–242.
9. Balog, R.; Jorgensen, B.; Nilsson, L.; Andersen, M.; Rienks, E.; Bianchi, M.; Fanetti, M.; Laegsgaard, E.; Baraldi, A.; Lizzit, S.; *et al*. Bandgap Opening in Graphene Induced by Patterned Hydrogen Adsorption. *Nat. Mater.* **2010**, *9*, 315–319.
10. Lahiri, J.; Lin, Y.; Bozkurt, P.; Oleynik, I. I.; Batzill, M. An Extended Defect in Graphene as a Metallic Wire. *Nat. Nanotechnol.* **2010**, *5*, 326–329.
11. Zhou, S. Y.; Gweon, G. H.; Fedorov, A. V.; First, P. N.; De Heer, W. A.; Lee, D. H.; Guinea, F.; Neto, A. H. C.; Lanzara, A. Substrate-Induced Bandgap Opening in Epitaxial Graphene. *Nat. Mater.* **2007**, *6*, 770–775.
12. Giovannetti, G.; Khomyakov, P. A.; Brocks, G.; Karpan, V. M.; van den Brink, J.; Kelly, P. J. Doping Graphene with Metal Contacts. *Phys. Rev. Lett.* **2008**, *101*, 026803.
13. Chang, H. X.; Cheng, J. S.; Liu, X. Q.; Gao, J. F.; Li, M. J.; Li, J. H.; Tao, X. M.; Ding, F.; Zheng, Z. J. Facile Synthesis of Wide-bandgap Fluorinated Graphene Semiconductors. *Chem.—Eur. J.* **2011**, *17*, 8896–8903.
14. Wei, Z. Q.; Wang, D. B.; Kim, S.; Kim, S. Y.; Hu, Y. K.; Yakes, M. K.; Laracuente, A. R.; Dai, Z. T.; Marder, S. R.; Berger, C.; *et al*. Nanoscale Tunable Reduction of Graphene Oxide for Graphene Electronics. *Science* **2010**, *328*, 1373–1376.
15. Wu, X. S.; Sprinkle, M.; Li, X. B.; Ming, F.; Berger, C.; de Heer, W. A. Epitaxial-Graphene/Graphene-Oxide Junction: An Essential Step Towards Epitaxial Graphene Electronics. *Phys. Rev. Lett.* **2008**, *101*, 026801.
16. Nair, R. R.; Blake, P.; Grigorenko, A. N.; Novoselov, K. S.; Booth, T. J.; Stauber, T.; Peres, N. M. R.; Geim, A. K. Fine Structure Constant Defines Visual Transparency of Graphene. *Science* **2008**, *320*, 1308.
17. Wang, F.; Zhang, Y. B.; Tian, C. S.; Girit, C.; Zettl, A.; Crommie, M.; Shen, Y. R. Gate-Variable Optical Transitions in Graphene. *Science* **2008**, *320*, 206–209.
18. Wang, X.; Zhi, L. J.; Müllen, K. Transparent, Conductive Graphene Electrodes for Dye-Sensitized Solar Cells. *Nano Lett.* **2008**, *8*, 323–327.
19. Kim, K. S.; Zhao, Y.; Jang, H.; Lee, S. Y.; Kim, J. M.; Kim, K. S.; Ahn, J. H.; Kim, P.; Choi, J. Y.; Hong, B. H. Large-Scale Pattern Growth of Graphene Films for Stretchable Transparent Electrodes. *Nature* **2009**, *457*, 706–710.
20. Eda, G.; Fanchini, G.; Chhowalla, M. Large-Area Ultrathin Films of Reduced Graphene Oxide as a Transparent and Flexible Electronic Material. *Nat. Nanotechnol.* **2008**, *3*, 270–274.
21. Xia, F. N.; Mueller, T.; Lin, Y. M.; Valdes-Garcia, A.; Avouris, P. Ultrafast Graphene Photodetector. *Nat. Nanotechnol.* **2009**, *4*, 839–843.
22. Mueller, T.; Xia, F. N. A.; Avouris, P. Graphene Photodetectors for High-Speed Optical Communications. *Nat. Photonics* **2010**, *4*, 297–301.
23. Bonaccorso, F.; Sun, Z.; Hasan, T.; Ferrari, A. C. Graphene Photonics and Optoelectronics. *Nat. Photonics* **2010**, *4*, 611–622.
24. Chang, H. X.; Sun, Z. H.; Yuan, Q. H.; Ding, F.; Tao, X. M.; Yan, F.; Zheng, Z. J. Thin Film Field-Effect Phototransistors from Bandgap-Tunable, Solution-Processed, Few-Layer Reduced Graphene Oxide Films. *Adv. Mater.* **2010**, *22*, 4872–4876.
25. Chang, H. X.; Wang, G. F.; Yang, A.; Tao, X. M.; Liu, X. Q.; Shen, Y. D.; Zheng, Z. J. A Transparent, Flexible, Low-Temperature, and Solution-Processible Graphene Composite Electrode. *Adv. Funct. Mater.* **2010**, *20*, 2893–2902.
26. Chang, H. X.; Wu, H. K. Graphene-Based Nanomaterials: Synthesis, Properties and Optical and Optoelectronic Applications. *Adv. Funct. Mater.* **2013**, *23*, 1984–1997.
27. Chang, H. X.; Tang, L. H.; Wang, Y.; Jiang, J. H.; Li, J. H. Graphene Fluorescence Resonance Energy Transfer Aptasensor for the Thrombin Detection. *Anal. Chem.* **2010**, *82*, 2341–2346.
28. Kim, D. W.; Kim, Y. H.; Jeong, H. S.; Jung, H. T. Direct Visualization of Large-Area Graphene Domains and Boundaries by Optical Birefringency. *Nat. Nanotechnol.* **2012**, *7*, 29–34.
29. Echtermeyer, T. J.; Britnell, L.; Jasnos, P. K.; Lombardo, A.; Gorbachev, R. V.; Grigorenko, A. N.; Geim, A. K.; Ferrari, A. C.; Novoselov, K. S. Strong Plasmonic Enhancement of Photovoltage in Graphene. *Nat. Commun.* **2011**, *2*, 458.
30. Song, J. C. W.; Rudner, M. S.; Marcus, C. M.; Levitov, L. S. Hot Carrier Transport and Photocurrent Response in Graphene. *Nano Lett.* **2011**, *11*, 4688–4692.
31. Bao, Q. L.; Zhang, H.; Wang, B.; Ni, Z. H.; Lim, C. H. Y. X.; Wang, Y.; Tang, D. Y.; Loh, K. P. Broadband Graphene Polarizer. *Nat. Photonics* **2011**, *5*, 411–415.
32. Lemme, M. C.; Koppens, F. H. L.; Falk, A. L.; Rudner, M. S.; Park, H.; Levitov, L. S.; Marcus, C. M. Gate-Activated Photoresponse in a Graphene p-n Junction. *Nano Lett.* **2011**, *11*, 4134–4137.
33. Sun, D.; Divin, C.; Rioux, J.; Sipe, J. E.; Berger, C.; de Heer, W. A.; First, P. N.; Norris, T. B. Coherent Control of Ballistic Photocurrents in Multilayer Epitaxial Graphene Using Quantum Interference. *Nano Lett.* **2010**, *10*, 1293–1296.
34. Crassee, I.; Levallois, J.; Walter, A. L.; Ostler, M.; Bostwick, A.; Rotenberg, E.; Seyller, T.; van der Marel, D.; Kuzmenko, A. B. Giant Faraday Rotation in Single- and Multilayer Graphene. *Nat. Phys.* **2011**, *7*, 48–51.
35. Gabor, N. M.; Song, J. C. W.; Ma, Q.; Nair, N. L.; Taychatanapat, T.; Watanabe, K.; Taniguchi, T.; Levitov, L. S.; Jarillo-Herrero, P. Hot Carrier-Assisted Intrinsic Photoresponse in Graphene. *Science* **2011**, *334*, 648–652.
36. Lee, E. J. H.; Balasubramanian, K.; Weitz, R. T.; Burghard, M.; Kern, K. Contact and Edge Effects in Graphene Devices. *Nat. Nanotechnol.* **2008**, *3*, 486–490.
37. Park, J.; Ahn, Y. H.; Ruiz-Vargas, C. Imaging of Photocurrent Generation and Collection in Single-Layer Graphene. *Nano Lett.* **2009**, *9*, 1742–1746.
38. Liu, Y.; Cheng, R.; Liao, L.; Zhou, H.; Bai, J.; Liu, G.; Liu, L.; Huang, Y.; Duan, X. Plasmon Resonance Enhanced Multicolour Photodetection by Graphene. *Nat. Commun.* **2011**, *2*, 579.
39. Acik, M.; Lee, G.; Mattevi, C.; Chhowalla, M.; Cho, K.; Chabal, Y. J. Unusual Infrared-Absorption Mechanism in Thermally Reduced Graphene Oxide. *Nat. Mater.* **2010**, *9*, 840–845.
40. Xu, X. D.; Gabor, N. M.; Alden, J. S.; van der Zande, A. M.; McEuen, P. L. Photo-thermoelectric Effect at a Graphene Interface Junction. *Nano Lett.* **2010**, *10*, 562–566.
41. Sun, D.; Aivazian, G.; Jones, A. M.; Ross, J. S.; Yao, W.; Cobden, D.; Xu, X. D. Ultrafast Hot-Carrier-Dominated Photocurrent in Graphene. *Nat. Nanotechnol.* **2012**, *7*, 114–118.
42. Luo, Z. T.; Vora, P. M.; Mele, E. J.; Johnson, A. T. C.; Kikkawa, J. M. Photoluminescence and Band Gap Modulation in Graphene Oxide. *Appl. Phys. Lett.* **2009**, *94*, 111909.
43. Chien, C. T.; Li, S. S.; Lai, W. J.; Yeh, Y. C.; Chen, H. A.; Chen, I. S.; Chen, L. C.; Chen, K. H.; Nemoto, T.; Isoda, S.; *et al*. Tunable Photoluminescence from Graphene Oxide. *Angew. Chem., Int. Ed.* **2012**, *51*, 6662–6666.
44. Mattevi, C.; Eda, G.; Agnoli, S.; Miller, S.; Mkhoyan, K. A.; Celik, O.; Mostrogiovanni, D.; Granozzi, G.; Garfunkel, E.; Chhowalla, M. Evolution of Electrical, Chemical, and Structural Properties of Transparent and Conducting Chemically Derived Graphene Thin Films. *Adv. Funct. Mater.* **2009**, *19*, 2577–2583.
45. Stankovich, S.; Dikin, D. A.; Piner, R. D.; Kohlhaas, K. A.; Kleinhammes, A.; Jia, Y.; Wu, Y.; Nguyen, S. T.; Ruoff, R. S. Synthesis of Graphene-Based Nanosheets *via* Chemical Reduction of Exfoliated Graphite Oxide. *Carbon* **2007**, *45*, 1558–1565.
46. Bagri, A.; Mattevi, C.; Acik, M.; Chabal, Y. J.; Chhowalla, M.; Shenoy, V. B. Structural Evolution during the Reduction of Chemically Derived Graphene Oxide. *Nat. Chem.* **2010**, *2*, 581–587.
47. Lerf, A.; He, H. Y.; Forster, M.; Klinowski, J. Structure of Graphite Oxide Revisited. *J. Phys. Chem. B* **1998**, *102*, 4477–4482.

48. Yan, J. A.; Xian, L. D.; Chou, M. Y. Structural and Electronic Properties of Oxidized Graphene. *Phys. Rev. Lett.* **2009**, *103*, 086802.
49. Nair, R. R.; Ren, W. C.; Jalil, R.; Riaz, I.; Kravets, V. G.; Britnell, L.; Blake, P.; Schedin, F.; Mayorov, A. S.; Yuan, S. J.; *et al*. Fluorographene: A Two-Dimensional Counterpart of Teflon. *Small* **2010**, *6*, 2877–2884.
50. Yuan, Q. H.; Hu, H.; Gao, J. F.; Ding, F.; Liu, Z. F.; Yakobson, B. I. Upright Standing Graphene Formation on Substrates. *J. Am. Chem. Soc.* **2011**, *133*, 16072–16079.
51. Yuan, Q. H.; Gao, J. F.; Shu, H. B.; Zhao, J. J.; Chen, X. S.; Ding, F. Magic Carbon Clusters in the Chemical Vapor Deposition Growth of Graphene. *J. Am. Chem. Soc.* **2012**, *134*, 2970–2975.
52. Wang, J. L.; Ma, L.; Yuan, Q. H.; Zhu, L. Y.; Ding, F. Transition-Metal-Catalyzed Unzipping of Single-Walled Carbon Nanotubes into Narrow Graphene Nanoribbons at Low Temperature. *Angew. Chem., Int. Ed.* **2011**, *50*, 8041–8045.
53. Kaniyankandy, S.; Achary, S. N.; Rawalekar, S.; Ghosh, H. N. Ultrafast Relaxation Dynamics in Graphene Oxide: Evidence of Electron Trapping. *J. Phys. Chem. C* **2011**, *115*, 19110–19116.
54. Chitara, B.; Panchakarla, L. S.; Krupanidhi, S. B.; Rao, C. N. R. Infrared Photodetectors Based on Reduced Graphene Oxide and Graphene Nanoribbons. *Adv. Mater.* **2011**, *23*, 5419–5424.
55. Chen, X. P.; Zhu, H. L.; Cai, J. F.; Wua, Z. Y. High-performance 4H-SiC-Based Ultraviolet p-i-n Photodetector. *J. Appl. Phys.* **2007**, *102*, 024505.
56. Sun, Z. H.; Liu, Z. K.; Li, J. H.; Tai, G. A.; Lau, S. P.; Yan, F. Infrared Photodetectors Based on CVD-Grown Graphene and PbS Quantum Dots with Ultrahigh Responsivity. *Adv. Mater.* **2012**, *24*, 5878–5883.
57. Segal, M. Selling Graphene by the Ton. *Nat. Nanotechnol.* **2009**, *4*, 611–613.
58. Li, J. H.; Liu, D. Q.; Miao, Q.; Yan, F. The Application of a High-k Polymer in Flexible Low-Voltage Organic Thin-Film Transistors. *J. Mater. Chem.* **2012**, *22*, 15998–16004.